2-8-2019

Diagnostic Performance of Receptor-Specific Surgical Specimen Staining Correlates with Receptor Expression Level

Jasmin M. Schaefer
Oregon Health and Science University

Connor W. Barth
Oregon Health and Science University

Scott C. Davis
Dartmouth College

Summer L. Gibbs
Oregon Health and Science University

Journal of Biomedical Optics

BiomedicalOptics.SPIEDigitalLibrary.org

Diagnostic performance of receptor-specific surgical specimen staining correlates with receptor expression level

Jasmin M. Schaefer
Connor W. Barth
Scott C. Davis
Summer L. Gibbs

SPIE.

Jasmin M. Schaefer, Connor W. Barth, Scott C. Davis, Summer L. Gibbs, "Diagnostic performance of receptor-specific surgical specimen staining correlates with receptor expression level," *J. Biomed. Opt.* **24**(2), 026002 (2019), doi: 10.1117/1.JBO.24.2.026002.

Journal of Biomedical Optics 24(2), 026002 (February 2019)

Diagnostic performance of receptor-specific surgical specimen staining correlates with receptor expression level

Jasmin M. Schaefer,[a] Connor W. Barth,[a] Scott C. Davis,[b,*] and Summer L. Gibbs[a,c,d,*]
[a]Oregon Health and Science University, Department of Biomedical Engineering, Portland, Oregon, United States
[b]Thayer School of Engineering, Dartmouth College, Hanover, New Hampshire, United States
[c]Oregon Health and Science University, Knight Cancer Institute, Portland, Oregon, United States
[d]Oregon Health and Science University, OHSU Center for Spatial Systems Biomedicine, Portland, Oregon, United States

Abstract. Intraoperative margin assessment is imperative to cancer cure but is a continued challenge to successful surgery. Breast conserving surgery is a relevant example, where a cosmetically improved outcome is gained over mastectomy, but re-excision is required in >25% of cases due to positive or closely involved margins. Clinical translation of margin assessment modalities that must directly contact the patient or required administered contrast agents are time consuming and costly to move from bench to bedside. Tumor resections provide a unique surgical opportunity to deploy margin assessment technologies including contrast agents on the resected tissues, substantially shortening the path to the clinic. However, staining of resected tissues is plagued by nonspecific uptake. A ratiometric imaging approach where matched targeted and untargeted probes are used for staining has demonstrated substantially improved biomarker quantification over staining with conventional targeted contrast agents alone. Our group has developed an antibody-based ratiometric imaging technology using fluorescently labeled, spectrally distinct targeted and untargeted antibody probes termed dual-stain difference specimen imaging (DDSI). Herein, the targeted biomarker expression level and pattern are evaluated for their effects on DDSI diagnostic potential. Epidermal growth factor receptor expression level was correlated to DDSI diagnostic potential, which was found to be robust to spatial pattern expression variation. These results highlight the utility of DDSI for accurate margin assessment of freshly resected tumor specimens. [DOI: 10.1117/1.JBO.24.2.026002]

Keywords: dual-stain difference specimen imaging; breast conserving surgery; paired agent imaging; image-guided surgery.

Paper 180616R received Nov. 7, 2018; accepted for publication Jan. 11, 2019; published online Feb. 8, 2019.

1 Introduction

Through implementation of widespread mammography screening programs in the United States, a substantial number of early stage breast cancers are now detected.[1,2] One of the most common treatments for early stage breast cancer is breast conserving surgery (BCS) or lumpectomy.[3] While cosmetically improved over mastectomy, BCS can have re-excision rates ranging from 23% to 38% due to close or involved tumor margins as determined through comprehensive histopathological analysis following surgery.[4,5] Any findings of close or involved margins require immediate follow-up surgery, which increases patient stress and risk of morbidity, reducing the likelihood of a positive outcome.[6–9] Thus, it is important that the entire tumor is removed during the primary surgery to minimize re-excision rates as well as risk for local recurrence.[10] A number of intraoperative margin analysis technologies have been developed to reduce re-excision rates, including frozen section analysis and touch prep cytology, which have been deployed clinically.[11,12] However, none of the current intraoperative margin assessment techniques have been able to counter the current re-excision rate due to lack of sensitivity and specificity and/or challenges in adopting these procedures into the standard surgical workflow.[13–18] Therefore, the need for a robust, accurate intraoperative margin assessment technology to guide BCS remains.

To address this challenge, several groups have examined the utility of tissue staining techniques on resected specimens to help identify positive margins during surgery. One such technique, which we termed dual-stain difference specimen imaging (DDSI), involves the use of a biomarker-targeted fluorescent probe and a spectrally distinct untargeted isotype control probe to normalize the images and emphasize targeted-probe binding.[19–26] A variety of probes have been examined for this application by our group and others, including epidermal growth factor receptor (EGFR), human epidermal growth factor receptor 2 (HER2), estrogen receptor (ER), and CD44, where targeting the extracellular domain of receptors has shown the best performance.[19,20,25] Previously, we reported on an extensive staining optimization study for HER2-targeted DDSI. This study resulted in a DDSI staining methodology that accurately reported HER2-specific expression, predicting tumor tissue from normal adipose tissue with 91% sensitivity and 84% specificity on a testing data set of both high and low HER2-expressing tumors.[19] However, the relationship between DDSI performance and the expression level of the targeted biomarker has yet to be examined and quantified.

In this work, we used receiver operator characteristic (ROC) curve analysis to examine the relationship between receptor expression level and diagnostic performance of DDSI in tumors with varying levels of EGFR expression, a receptor overexpressed

*Address all correspondence to Scott C. Davis E-mail: Scott.C.Davis@Dartmouth.edu; Summer L. Gibbs, E-mail: gibbss@ohsu.edu

in some triple negative breast cancers.[27] Three cell lines with varied EGFR expression were grown as xenografts in the murine mammary adipose pads as a model system to evaluate DDSI contrast following resection of tumors with varied biomarker expression levels. In addition, we examined the effect of tumor biomarker spatial heterogeneity on the diagnostic performance of DDSI in these model systems using ROC curve analysis.

2 Materials and Methods

2.1 *General Study Design*

1. The previously optimized DDSI protocol[19] was applied to xenografts derived from cell lines with varied levels of EGFR expression, and the diagnostic performance was quantified using ROC curve analysis.
2. The optimal DDSI analysis method for biomarker heterogeneity was assessed, where standard cumulative tissue analysis was compared to cumulative and concentric ring analyses. ROC curve analysis was used to determine diagnostic performance of each method for optimal use in future studies.

Each tumor xenograft replicate was compared to surrounding mammary adipose and muscle tissues for diagnostic potential ($n = 20$ tumor–normal tissue pairs per cell line), resulting in a total of 60 tumor–normal tissue pairs that were stained with the previously optimized DDSI protocol. Coregistered color, targeted, and untargeted probe images were captured using a custom-build, wide-field imaging system. DDSI image processing was completed using custom written MatLab code and DDSI diagnostic performance was evaluated using ROC curve analysis. Tissue type and EGFR expression levels were confirmed using gold standard hematoxylin and eosin (H&E) and immunohistochemistry (IHC) staining, respectively.

2.2 *Fluorophores and Antibodies*

Alexa Fluor 647 (AF647, Thermo Fisher Scientific, Waltham, Massachusetts) and Cy3B (GE Healthcare Life Sciences, Little Chalfont, United Kingdom) were purchased in their *N*-hydroxysuccinimidyl ester form and solubilized in anhydrous dimethyl sulfoxide (DMSO) at 10 mM for antibody conjugation. Cetuximab [Erbitux, Eli Lilly and Company, Branchburg, New Jersey, molecular weight (MW) = 152 kDa] was used as the targeted probe. Donkey anti-Rabbit IgG (DkRb, Jackson ImmunoResearch, West Grove, Pennsylvania, MW = 150 kDa) was used as the untargeted probe.

2.3 *Cell Lines and Flow Cytometry*

The human epidermoid carcinoma cell line A431, human pancreatic adenocarcinoma cell line AsPC-1, and human breast adenocarcinoma cell line MDA-MB-231 were cultured in DMEM 1× (Thermo Fisher Scientific) supplemented with 10% fetal bovine serum (FBS, Seradigm, Sanborn, New York) and 1% penicillin–streptomycin–glutamine (Thermo Fisher Scientific). All cell lines were grown to ~90% confluence prior to trypsinization and subsequent preparation for EGFR quantification by flow cytometry. The suspended cells were pelleted at 1000 rpm for 5 min prior to resuspension in 4% paraformaldehyde (PFA, Sigma-Aldrich, St. Louis, Missouri) for 15 min. The fixed cells were pelleted again to remove PFA, after which they were blocked in 5% FBS for 15 min. The cells were then stained with cetuximab conjugated to AF647 (fluorophore-to-protein conjugation ratio of 2 to 3 for flow cytometry studies) at 250-nM protein concentration for 2 h at room temperature. The stained cells were pelleted, washed three times with phosphate buffered saline (PBS), fixed in 4% PFA for 15 min, and washed three additional times with PBS. The stained cell pellets were resuspended in PBS to a final concentration of 1×10^6 cells/mL, where triplicate samples per cell line were quantified using flow cytometry. Additional unstained cells were prepared for each cell line as a negative control in triplicate per cell line.

All flow cytometry experiments were conducted on a Becton Dickinson LSRII (Becton Dickinson Company, Franklin Lakes, New Jersey) flow cytometer. The flow cytometer was configured with a 633 (660/20) Cy5 channel, which was used to detect AF647 (excitation maximum: 650 nm, emission maximum: 665 nm). Prior to analyzing cells, Quantum™ AF647 molecular equivalents of soluble fluorophore beads (Bangs Laboratories, Inc., Fishers, Indiana) were analyzed to enable receptor-based quantification of EGFR per cell. 10,000 cells per samples were counted and the data were analyzed using FlowJo software (FlowJo, LLC, Ashland, Oregon).

2.4 *Mice, Tumor Implantation, and Growth*

All animal studies were approved by the Institutional Animal Care and Use Committee at Oregon Health and Science University (OHSU). Female athymic nude mice (32 to 38 days old, homozygous 490, Charles River Laboratories, Wilmington, Massachusetts) weighing 19 to 21 g were used to grow xenografts of each of the three selected cell lines. Mice were anesthetized using 100 mg/kg ketamine (Hospira Inc., Lake Forest, Illiois) and 10 mg/kg xylazine (AnaSed, Shenandoah, Iowa) administered by intraperitoneal injection. Depth of anesthesia was accessed using the toe pinch method prior to tumor implantation.

In a sterile field, the peritoneal area was sterilized using povidone-iodine (Purdue Products, Stamford, Connecticut). A small incision (3 to 5 mm) was made along the lateral side of each inferior nipple. Using forceps, mammary adipose was extracted though the incision and 200 μL of cell suspension (1×10^6 cells) were injected. The mammary adipose was inserted back through the incision, and it was sealed with Vetbond™ (3M, St. Paul, Minnesota). Mice were monitored daily following the procedure to ensure healing for 5 to 7 days and then weekly for tumor growth and overall health.

Tumors were allowed to grow to a maximum size of 1.5 cm^3 which was reached in 10 to 14 days for A431, 4 to 5 weeks for AsPC-1, and 3 to 4 weeks for MDA-MB-231 xenografts. Each cell line was implanted into a cohort of five mice, where two tumors per mouse were implanted. This resulted in $n = 20$ tumor samples per cell line following bisection of the resected tumor prior to DDSI staining.

2.5 *Antibody–Fluorophore Conjugations*

Cetuximab was conjugated to AF647, and DkRb was conjugated to Cy3B. Antibody conjugations to their respective fluorophore were completed as previously described.[19] The fluorophore-to-protein ratio of each conjugate was quantified using absorbance spectroscopy (SpectraMax M5, Molecular Devices, San Jose, California) with the antibody absorbance

measured at 280 nm [cetuximab and DkRb extinction coefficient (ε) = 210,000 M^{-1} cm^{-1}], Cy3B absorbance measured at 560 nm (Cy3B ε = 130,000 M^{-1} cm^{-1}), and AF647 absorbance measured at 650 nm (AF647 ε = 270,000 M^{-1} cm^{-1}). All fluorophore-to-antibody ratios were between 3:1 and 4:1 for DDSI staining studies. The DDSI staining solution was made from a mixture of the cetuximab-AF647 and DkRb-Cy3B conjugates in 1× PBS, pH 7.4, 0.1% Tween 20, and 1% bovine serum albumin (BSA) at a final concentration 200 nM of each antibody as measured by protein concentration.

2.6 *Tumor Resection and DDSI Staining*

All mice were euthanized using carbon dioxide asphyxiation followed by cervical dislocation. Tumors were excised and bisected resulting in two samples from each tumor. For each tumor sample, a corresponding mammary adipose sample was harvested from the chest, and a muscle sample was harvested from the posterior thigh of each mouse. Each tumor, adipose, and muscle group was stained and washed together following the previously published DDSI staining procedure,[19] described in brief as follows. Tumor and normal tissues were blocked by incubating in 1 mL of 2% BSA in 1× PBS for 10 min, followed by a 1-min incubation in 1 mL of 200 nM cetuximab-AF647 and DkRb-Cy3B. The stained tissue samples were then washed in 50 mL of 0.1% Tween-20 in 1× PBS under gentle agitation for 5 min. The stained tumor and normal tissues were imaged on glass slides with the bisected side facing the light source and camera.

2.7 *DDSI Macroscopic Imaging*

Color and fluorescence images of tumor and normal tissue pairs were collected using a previously described custom-built wide field imaging system,[28] detailed briefly as follows. The macroscopic fluorescence imaging system consisted of a QImaging EXi Blue monochrome camera (Surrey, British Columbia, California) with a removable Bayer filter and a PhotoFluor II light source (89 North, Burlington, Vermont). The light source was outfitted with 545 ± 12.5 nm or 620 ± 30 nm bandpass excitation filter for Cy3B or AF647, respectively. A 605 ± 35 nm or a 700 ± 37.5 nm bandpass emission filter was placed in front of the camera for detection of Cy3B or AF647 fluorescence emission, respectively. All filters were obtained from Chroma Technology (Bellows Falls, Vermont). An aliquot of the staining solution was placed in a covered optical well plate (Greiner Bio-One, Monroe, North Carolina) and imaged with each tumor and normal tissue pair for image calibration.

2.8 *DDSI Processing*

The targeted and untargeted fluorescence images were used to calculate DDSI using custom written MatLab code (MathWorks, Natick, Massachusetts) described briefly as follows. Regions of interest (ROIs) were selected for background signal in which median signal was subtracted from the entire image. An ROI was also selected from the DDSI staining solution for intensity normalization between fluorescence channels, where each pixel value in each fluorescence image was divided by the average intensity value of the ROI selected within the DDSI staining solution. Tumor or normal tissue ROIs were selected using white light images and used to mask each fluorescence image. DDSI was calculated as $I_{DDSI} = (I_{Targeted} - I_{Untargeted})/I_{Untargeted}$, where I is the fluorescence signal intensity.

2.9 *IHC Staining and Microscopy*

Immediately after completion of the DDSI stain protocol, each tumor and normal tissue pair was flash frozen in optimal cutting temperature (Fisher HealthCare, Houston, Texas) compound for tissue preservation and to maintain tumor orientation. All tissue blocks were sent to the OHSU Histology Shared Resource Core where they were thawed and re-embedded in paraffin, maintaining tissue orientation. The formalin-fixed paraffin embedded tissue blocks were faced prior to collection of a representative section of the tumor, adipose, and muscle pieces. IHC staining was performed on 4-μm sections using an EGFR antibody (1:300, clone EP38Y, AbCam, Cambridge, Massachusetts) targeted to a different epitope to prevent steric hindrance with pre-existing labeling from cetuximab. Serial sections were used for gold standard H&E staining. Due to the tissue processing and sectioning necessary to generate sections of the tumor, muscle, and adipose pieces, the same tissue face that was imaged macroscopically using DDSI was not able to be sampled microscopically. However, the IHC- and H&E-stained sections provide representative EGFR expression and necrotic region tissue maps, respectively, for each tumor. Bright field images of all IHC- and H&E-stained slides were collected at 10× magnification using the Zeiss AxioScan.Z1 (Carl Zeiss Microscopy GmbH, Jena, Germany). ROIs of the IHC and H&E slides were detected using the Automatic Tissue Recognition feature in the ZEN software (Zeiss). Six fields of view were used to set the focus map prior to image scanning and tiling of each H&E- and IHC-stained sections.

2.10 *Statistical Analysis*

As previously described, statistical analysis was performed using MatLab.[19] In brief, tumor-to-normal tissue diagnostic detection was assessed through the calculation of ROC curves from DDSI. ROC curves and corresponding area under the curve (AUC) measurement were calculated using MatLab on a pixel-by-pixel basis. Briefly, a threshold variable was generated with a linearly increasing value from the minimum to maximum pixel intensity value. The threshold variable was then used to generate the true-positive rate (% of tumor pixels greater than the threshold, TPR), false-positive rate (% of normal pixels less than the threshold, FPR), ROC curves, and the corresponding AUC values by plotting these values at each threshold value. Three methods were employed to select the tumor pixels used to quantify the DDSI ROC curves including (1) standard cumulative tissue analysis as previously described,[19] (2) cumulative ring analysis, and (3) concentric ring analysis. For the (1) standard cumulative tissue analysis, tumor pixel values were taken from the entire tumor tissue area and used for ROC analysis of tumor versus normal tissue diagnostic potential. For the (2) cumulative ring analysis, an iterative analysis was completed, where tumor pixel values were taken from rings starting at the edge of the tumor (0.1 mm in depth), where the ring depth was increased by 0.1 mm for each iteration. The cumulative rings were moved into the tumor up to 3 mm from the edge and progressively more tumor pixels from the edge were included in the ROC curve analysis to differentiate tumor versus normal tissue. For the (3) concentric ring analysis, an iterative analysis was completed where tumor pixel values

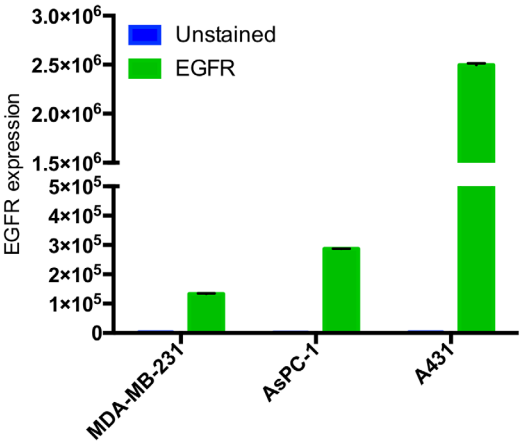

Fig. 1 Quantified EGFR expression Levels. EGFR expression was quantified *in vitro* via flow cytometry using cetuximab directly labeled with AF647. The autofluorescence level of each cell line was quantified as a negative control on unstained cells.

were taken from rings starting at the edge of the tumor at a set width of 0.1 mm. The ring location was moved concentrically inward up to 3 mm from the tumor edge, where only the tumor pixels contained within the 0.1-mm wide ring at the specific depth from the tumor edge were used in the tumor versus normal tissue ROC curve analysis. Both the cumulative and concentric ring analysis methods utilized the MatLab imerode function to obtain regular rings with minimal variation upon further inclusion. Normal tissue pixel values were taken from the entire normal tissue area in all analysis methods.

3 Results

3.1 *Diagnostic Performance of DDSI Correlates with EGFR Expression Level*

Three cell lines with varied EGFR expression (A431, AsPC-1, and MDA-MB-231) were used to characterize the relationship between diagnostic performance of DDSI staining and biomarker overexpression level. A431 cells had the highest EGFR expression (2.5×10^6 receptors/cell), AsPC-1 cells had mid-level EGFR expression (2.9×10^5 receptors/cell), and MDA-MB-231 cells had the lowest EGFR expression (1.3×10^5 receptors/cell, Fig. 1). Qualitative assessment of calculated DDSI as compared to the targeted and untargeted fluorescence images showed an improved match between signal intensity and biomarker expression as determined by gold standard H&E and IHC. Comparison of the targeted and untargeted fluorescence images with the corresponding IHC and H&E demonstrated that the targeted and untargeted probes uptake was highest in the necrotic regions, which was corrected using DDSI calculations (Fig. 2). DDSI for the lower EGFR-expressing AsPC-1 and MDA-MB-231 xenografts were plotted on the same scale as the highly EGFR-expressing A431 tumors, where DDSI intensity was not as obvious for the lower EGFR-expressing tumors (Fig. 2). However, examination of a cohort of representative DDSI, H&E, and IHC images from each tumor

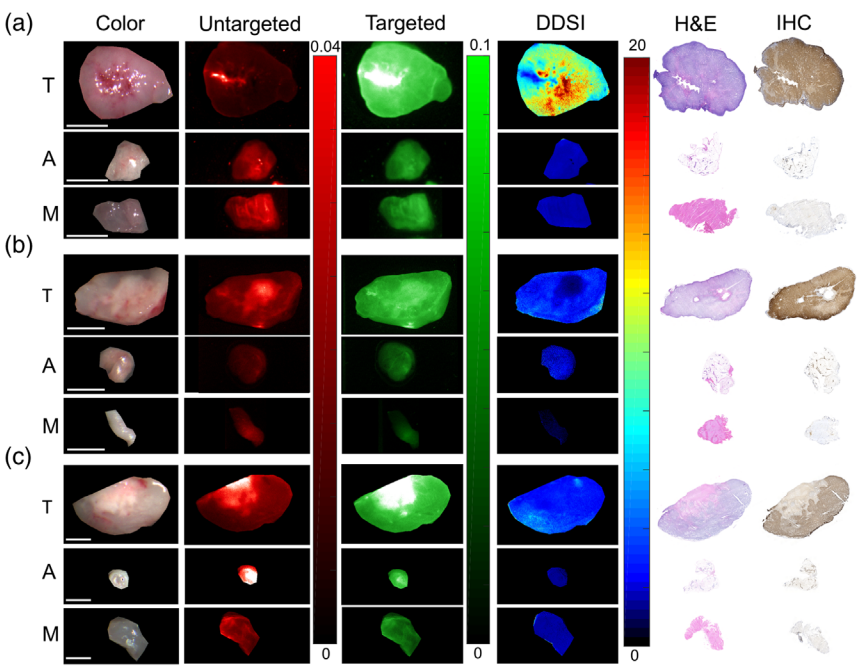

Fig. 2 Representative staining patterns from varied EGFR-expressing xenografts. A representative (a) A431, (b) AsPC-1, and (c) MDA-MB-231 tumor and corresponding mammary adipose and muscle tissue are shown as color, untargeted fluorescence, targeted fluorescence, DDSI, H&E-, and EGFR-stained IHC. All images are representative of $n = 20$ tumor, mammary adipose, and muscle tissue sets per tumor type. The untargeted and targeted fluorescence images were background corrected using their exposure time(s) and calibration drop intensities. An equivalent color scale, optimal for A431 xenografts, was used to display untargeted, targeted, and DDSI calculated images. IHC and H&E images were collected via serial sections from formalin-fixed paraffin embedded tissue blocks. IHC, immunohistochemistry; H&E, hematoxylin and eosin; T, tumor; A, mammary adipose; M, muscle. Scale bar = 5 mm.

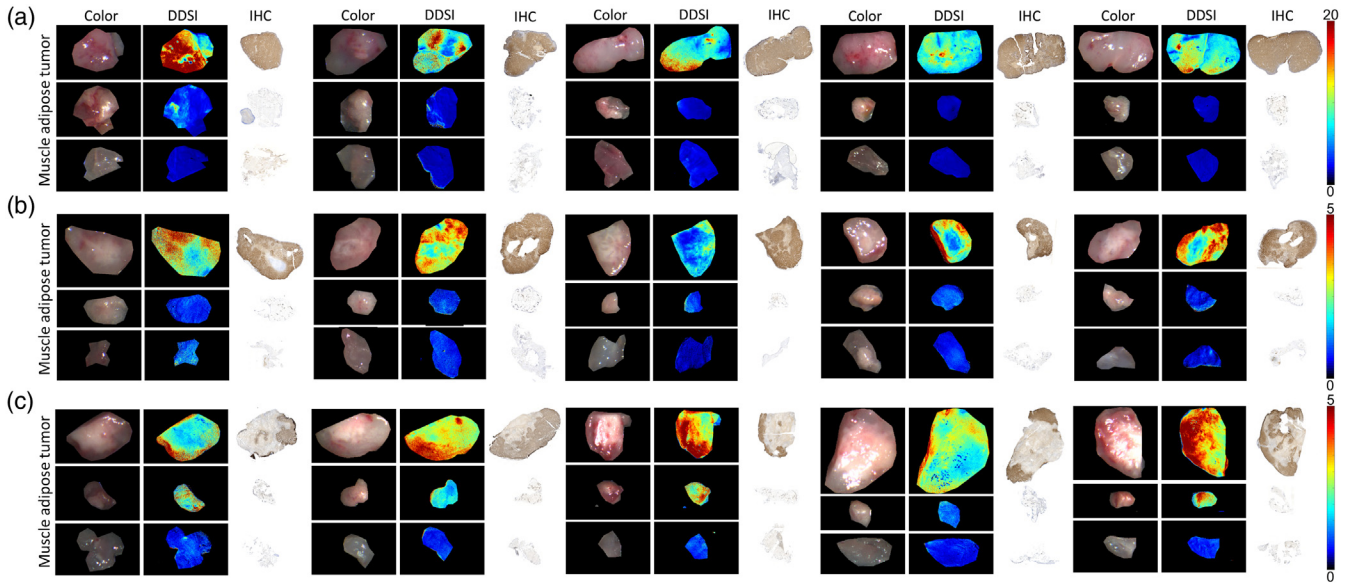

Fig. 3 DDSI staining validation and IHC analysis. A cohort of representative images from (a) A431, (b) AsPC-1, and (c) MDA-MB-231 tumors, mammary adipose, and muscle tissues are shown in color, DDSI, and EGFR-stained IHC. All images are representative of $n = 20$ tumor, mammary adipose, and muscle tissue sets per tumor type. DDSI calculated images are displayed on their respective optimal scale for each tumor type (see color bars on the right). IHC, immunohistochemistry.

type showed that DDSI intensity was representative of biomarker expression, when each tumor type was plotted on its optimal intensity scale (Fig. 3). Additionally, EGFR expression patterns were found to differ across xenograft types. The A431 tumors showed relatively homogeneous EGFR expression [Figs. 2(a) and 3(a)]. By comparison, the AsPC-1 and MDA-MB-231 tumors both showed heterogeneous EGFR expression with notable necrotic regions, where there were either minimal cells or minimal EGFR expression [Figs. 2(b) and 2(c)], which was true throughout the sample population [Figs. 3(b) and 3(c)].

Tumor-to-adipose and tumor-to-muscle DDSI diagnostic potential was quantitatively evaluated using ROC curve analysis for all A431, AsPC-1, and MDA-MB-231 replicates, where the AUC was used as the metric for comparison between xenografts. ROC curves for the tumor-to-adipose DDSI showed high diagnostic potential for the A431 tumors [AUC = 0.95, Fig. 4(a)], which had both relatively homogeneous EGFR expression as well as the highest EGFR expression level compared to the AsPC-1 or MDA-MB-231 tumors (Figs. 2 and 3). The EGFR expression level was well correlated with tumor-to-adipose DDSI diagnostic potential as demonstrated by the AUC for the three cells lines (AUC: A431 = 0.95, AsPC-1 = 0.91, and MDA-MB-231 = 0.67). However, this correlation was not linear as the EGFR expression level of the A431 cells was an order of magnitude higher than AsPC-1 cells (Fig. 1), and the DDSI AUCs were relatively similar between these two tumor types. Notably, the MDA-MB-231 xenografts, which had roughly half the EGFR expression of the AsPC-1 tumors, showed considerably lower tumor-to-adipose DDSI diagnostic potential based on the AUC [Fig. 4(a)]. ROC curves for the tumor-to-muscle DDSI ratios were substantially improved over the tumor-to-adipose DDSI ratios, where AUCs for all tumor xenografts were $\geq$0.95 [Fig. 4(b)]. When the ROC curve calculated AUC values for each replicate were evaluated, the standard deviation for the tumor-to-adipose DDSI was substantially larger than the tumor-to-muscle DDSI. In addition, the standard deviation increased with decreasing EGFR expression [Fig. 4(c)]. The ROC curve calculated AUC for tumor-to-adipose and tumor-to-muscle contrast for the targeted and untargeted channels alone were not well correlated with EGFR expression levels [Figs. 4(d)–4(h)]. Tumor-to-adipose ROC curve calculated AUC was higher for the targeted channel than for DDSI for the lower EGFR-expressing AsPC-1 and MDA-MB-231 tumor lines, demonstrating the incongruent quantification by comparison to the EGFR expression level (Figs. 1 and 4). In addition, when ROC curve calculated AUC values for each replicate were considered for the targeted [Fig. 4(f)] and untargeted [Fig. 4(I)] probes alone, much larger standard deviation was seen than for the ROC curve calculated AUC for the DDSI [Fig. 4(c)], showing the enhanced consistency in tumor-to-normal tissue contrast using DDSI instead of targeted probe staining alone.

3.2 *Necrotic Tissue Does Not Substantially Alter DDSI Diagnostic Potential*

The effect of the calculated ROC curve AUC DDSI variability [Fig. 4(c)] and observed necrotic regions in the AsPC-1 and MDA-MB-231 tumors (Figs. 2 and 3) was further investigated. The influence of these necrotic regions and thus heterogeneous EGFR expression on DDSI was assessed by comparing three DDSI analysis techniques including (1) standard cumulative tissue analysis (Fig. 4), (2) cumulative ring analysis (Fig. 5), and (3) concentric ring analysis (Fig. 6). The cumulative ring analysis was performed by drawing concentric circles at intervals of 0.1 mm from the edge of each tumor for up to a total depth of 3 mm into the tumor, where each subsequent DDSI analysis included the previous 0.1 mm (Fig. 5). This analysis method served to omit much of the necrotic regions of the AsPC-1 and MDA-MB-231 tumors from the DDSI analysis. DDSI ROC curve calculated AUC at 2 mm showed no increase in AUC for the A431 tumors compared to the cumulative tissue

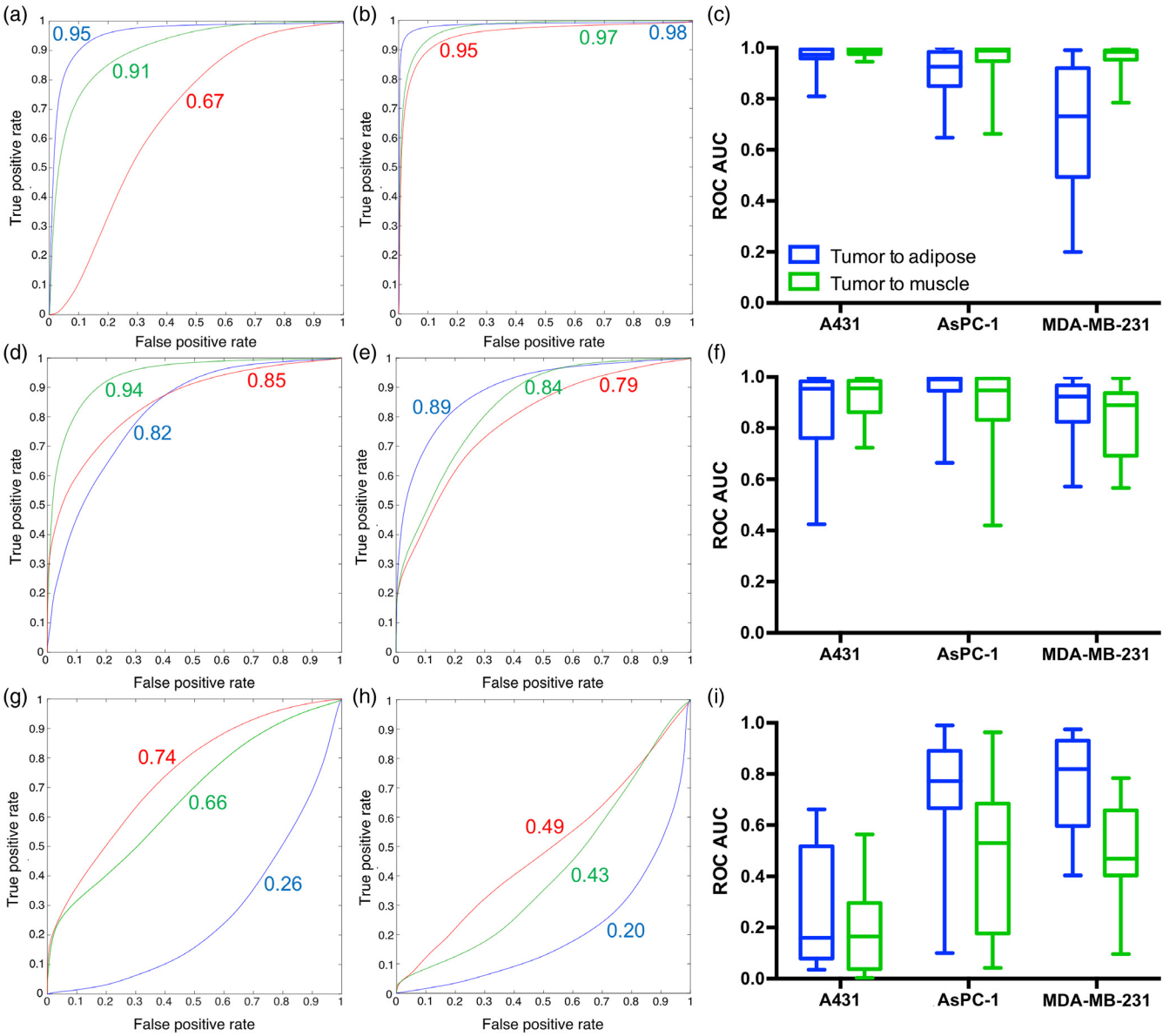

Fig. 4 Cumulative tissue analysis ROC curves and calculated AUC of varied EGFR-expressing xenografts. The lumped DDSI (a) tumor to adipose and (b) tumor to muscle cumulative tissue ROC curves for A431 (blue), AsPC-1 (green), and MDA-MB-231 (red) xenografts are shown for $n = 20$ tumor-to-adipose or tumor-to-muscle tissue pairs per cell line, respectively. (c) The DDSI ROC curve calculated AUC values for each of the 20 tumor-to-adipose and tumor-to-muscle pairs per cell line are plotted where the median, interquartile range, and standard deviation are shown. The lumped targeted (d) tumor-to-adipose and (e) tumor-to-muscle cumulative tissue ROC curves for A431 (blue), AsPC-1 (green), and MDA-MB-231 (red) xenografts are shown for $n = 20$ tumor-to-adipose or tumor-to-muscle tissue pairs per cell line, respectively. (f) The targeted ROC curve calculated AUC values for each of the 20 tumor-to-adipose and tumor-to-muscle pairs per cell line are plotted where the median, interquartile range, and standard deviation are shown. The lumped untargeted (g) tumor-to-adipose and (h) tumor-to-muscle cumulative tissue ROC curves for A431 (blue), AsPC-1 (green), and MDA-MB-231 (red) xenografts are shown for $n = 20$ tumor-to-adipose or tumor-to-muscle tissue pairs per cell line, respectively. (i) The untargeted ROC curve calculated AUC values for each of the 20 tumor-to-adipose and tumor-to-muscle pairs per cell line are plotted where the median, interquartile range, and standard deviation are shown. ROC, receiver operator characteristic; AUC, area under the curve.

analysis, whereas only a slight increase was seen for the AsPC-1 and MDA-MB-231 tumors [Figs. 5(a)–5(c)]. Notably, at the 2-mm depth of edge, the standard deviation between the ROC curve calculated AUCs of the tumor-to-adipose and tumor-to-muscle for each tumor line were substantially decreased compared to the cumulative tissue analysis [Figs. 4(c) and 5(d)]. Marginal change was seen in ROC curve calculated AUC using the cumulative tissue analysis method at up to 3 mm depth of edge (0.1 to 3 mm ROC calculated AUC range for tumor-to-adipose contrast: A431 = 0.88 to 0.95, AsPC-1 = 0.92 to 0.93, and MDA-MB-231 = 0.67 to 0.71) and thus, the 2-mm depth was selected as a representative example.

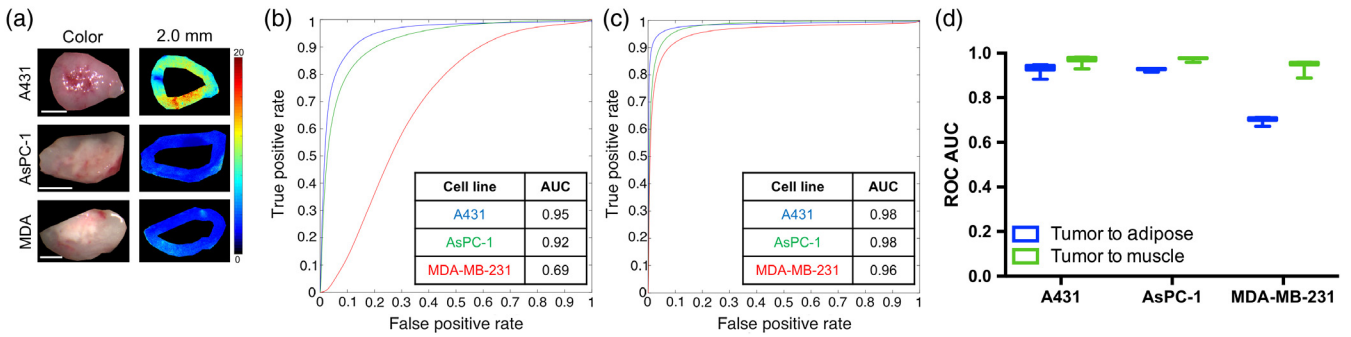

Fig. 5 Cumulative ring analysis ROC curves and calculated AUC of varied EGFR-expressing xenografts. Cumulative ring ROC curve analysis was employed at iterations of 0.1 mm intervals from the tumor edge with 2 mm cumulative analysis shown as a representative example. (a) Representative color and DDSI calculated images from each tumor type with DDSI shown on the optimal scale for A431 tumors. The lumped (b) tumor-to-adipose and (c) tumor-to-muscle ROC curve cumulative ring analysis at 2 mm is shown for $n = 20$ A431 (blue), AsPC-1 (green), and MDA-MB-231 (red) tumors. (d) The ROC curve calculated AUC values for each of the 20 tumor-to-adipose and tumor-to-muscle pairs per cell line are plotted where the median, interquartile range, and standard deviation are shown. ROC, receiver operator characteristic; AUC, area under the curve; scale bar = 5 mm.

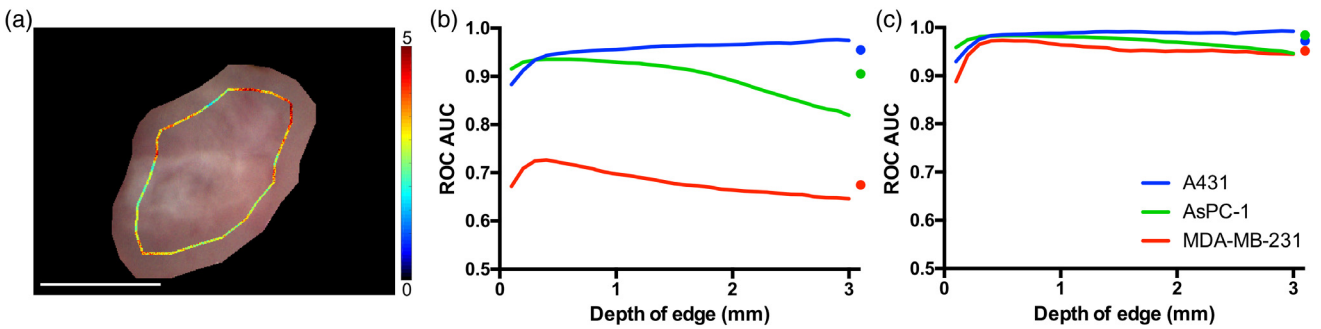

Fig. 6 Concentric ring analysis ROC curves calculated AUCs of varied EGFR-expressing xenografts. (a) Concentric ring ROC curve analysis was employed at iterations of 0.1 mm from the tumor edge up to 3 mm into each tumor sample, where DDSI of each ring was quantified individually. A representative example DDSI ring is shown. The lumped (b) tumor-to-adipose and (c) tumor-to-muscle ROC curve calculated AUC values at varied depth from the edge of the tumor for A431 (blue), AsPC-1 (green), and MDA-MB-231 (red) were calculated and are displayed over the total depth of edge calculated. For reference, the standard cumulative tissue analysis ROC curve calculated AUC are shown as solid dots on the right-hand side of each plot. ROC, receiver operator characteristic; AUC, area under the curve; scale bar = 5 mm.

The concentric ring analysis was performed by assessing DDSI in concentric 0.1 mm rings drawn from the edge of the tumor and analyzed individually [Fig. 6(a)]. DDSI ROC curve calculated AUCs for the A431 tumors were slightly increased using this analysis method compared with analyzing DDSI for the cumulative tissue [Fig. 6(b)]. In contrast, the DDSI tumor-to-adipose ROC curve calculated AUCs were sharply decreased for the AsPC-1 and MDA-MB-231 tumors when the concentric rings were moved closer to the center of the tumor, where the bulk of the low EGFR expression was located [Figs. 3(b), 3(c), and 6(b)]. This DDSI trend was even apparent in the tumor-to-muscle ROC curve calculated AUC values for AsPC-1 tumors, which had been stable for the other analyses, although the difference between the AUC values was much smaller [Fig. 6(c)].

4 Discussion

The primary goal of this study was to understand how the targeted cancer biomarker expression level correlated to DDSI staining diagnostic accuracy for intraoperative margin assessment, with a focus on BCS. BCS is the preferred treatment method for early stage breast cancer due to its improved cosmetic results and equivalence in patient survival to mastectomy.[3] However, the prevalence of incomplete tumor removal and positive margin status remains problematic, where positive margin status is correlated with local recurrence.[2,6–9] While a variety of targeted contrast agents have been developed for intraoperative cancer delineation,[29–32] translation to the clinic is expensive and time consuming and to date few cancer-specific probes have been moved from bench to bedside.[33–35] To facilitate the use of fluorescence-guided surgery for intraoperative margin assessment, we have developed DDSI to stain resected tissues so the contrast agents never touch the patient, significantly shortening the path to the clinic. DDSI utilizes ratiometric imaging of matched biomarker targeted and untargeted probes, which enables quantitative correction for nonspecific probe uptake, a prevalent problem when staining resected tissue specimens.[19,20,22,25]

Using our previously optimized DDSI methodology,[19] we evaluated the accuracy of DDSI to differentiate between tumor and normal tissues (adipose or muscle) where model

tumors with varied biomarker expression were assessed (Fig. 1). In addition to varied EGFR expression levels, these tumor models also presented heterogeneous spatial patterns of biomarker expression (Figs. 2 and 3), facilitating quantification of the effect of biomarker expression on DDSI diagnostic potential. As expected, DDSI diagnostic potential increased with increasing EGFR expression level, where the highest EGFR-expressing xenografts showed the greatest ability to differentiate between benign and malignant tissues (Fig. 4). Interestingly, the ability to accurately differentiation between tumor and normal tissues was not linearly correlation with biomarker expression level. EGFR expression level differed 10-fold between the A431 and AsPC-1 tumors, but DDSI ROC curve calculated AUC was nearly equivalent. MDA-MB-231 tumor EGFR expression was about half that of the AsPC-1 tumors; however, the DDSI ROC curve calculated AUC was much worse for the MDA-MB-231 samples when the tumor to adipose diagnostic potential was considered (Figs. 1 and 4). Thus, a threshold in biomarker expression level for DDSI diagnostic potential may exist, where tumors with lower biomarker expression levels could not be readily distinguished from normal tissue using a single biomarker to generate DDSI. A possible solution to this difficulty would be to stain for multiple biomarkers, where cancers commonly overexpress multiple proteins that could be targeted. The DDSI ROC curve calculated AUC values also demonstrated that tumor-to-adipose diagnostic accuracy was substantially more challenging to generate as compared to tumor-to-muscle diagnostic accuracy. Tumor-to-muscle ROC curve calculated AUCs were similar for all three tumor types even though they differed in EGFR expression by up to ~20-fold (Fig. 4). This is an important point for the use of such technology to quantitatively determine margin status for BCS, where the surrounding normal tissue is largely mammary adipose. The current study demonstrates that comparison to the accurate surrounding normal tissue is vital for assessment of diagnostic accuracy of ratiometric imaging methods.

The effect of biomarker spatial heterogeneity on diagnostic accuracy of DDSI was also examined herein, where the three model tumor types showed both homogeneous (A431) and heterogeneous (AsPC-1 and MDA-MB-231) EGFR expression (Figs. 2 and 3). Importantly, DDSI diagnostic potential was found to be robust against biomarker expression heterogeneity, where the cumulative and concentric ring analyses resulted in similar DDSI ROC curve calculated AUC values (Figs. 4 and 5). The largest effect on DDSI diagnostic potential was seen when concentric ring analysis was directly overlapping with the necrotic tumor regions, which served to diminish ROC curve calculated AUC values (Fig. 6). Fortunately, necrotic tissue would not be expected in clinical BCS margin assessment,[36–38] demonstrating that robust diagnostic potential of the DDSI method would be anticipated when comparing to benign mammary adipose tissue.

In summary, the DDSI methodology is dependent on the targeted biomarker expression level for quantitative differentiation between benign and malignant tissues. However, DDSI shows robust diagnostic potential even with spatial variation in biomarker expression. Furthermore, there appears to be a threshold biomarker expression level required for accurate differentiation between benign and malignant tissues using DDSI especially in the case of comparing to normal adipose tissues. Additional studies to define the biomarker threshold for DDSI diagnostic potential are underway. Although these studies have focused on BCS, this work is readily extendable to other cancer types. Overall, the DDSI methodology provides a means for quantitative margin assessment on freshly resected specimens, permitting rapid clinical translation for improved patient outcomes.

Disclosures

The authors declare no competing financial interests.

Acknowledgments

We would like to thank Dr. Kimberley Samkoe, Dr. Margaret Folaron, and Mr. Rendy Strawbridge for insightful discussions. This work was funded by the National Cancer Institute (R01CA188491).

References

1. K. D. Miller et al., "Cancer treatment and survivorship statistics, 2016," *CA Cancer J. Clin.* **66**, 271–289 (2016).
2. J. F. Waljee et al., "Predictors of re-excision among women undergoing breast-conserving surgery for cancer," *Ann. Surg. Oncol.* **15**, 1297–1303 (2008).
3. M. Morrow, J. R. Harris, and S. J. Schnitt, "Surgical margins in lumpectomy for breast cancer: bigger is not better," *N. Engl. J. Med.* **367**, 79–82 (2012).
4. L. E. McCahill et al., "Variability in reexcision following breast conservation surgery," *J. Am. Med. Assoc.* **307**, 467–475 (2012).
5. M. Morrow et al., "Surgeon recommendations and receipt of mastectomy for treatment of breast cancer," *J. Am. Med. Assoc.* **302**, 1551–1556 (2009).
6. G. Freedman et al., "Patients with early stage invasive cancer with close or positive margins treated with conservative surgery and radiation have an increased risk of breast recurrence that is delayed by adjuvant systemic therapy," *Int. J. Radiat. Oncol. Biol. Phys.* **44**, 1005–1015 (1999).
7. L. Jacobs, "Positive margins: the challenge continues for breast surgeons," *Ann. Surg. Oncol.* **15**, 1271–1272 (2008).
8. R. Jeevan et al., "Reoperation rates after breast conserving surgery for breast cancer among women in England: retrospective study of hospital episode statistics," *Br. Med. J.* **345**, e4505 (2012).
9. L. G. Wilke et al., "Repeat surgery after breast conservation for the treatment of stage 0 to II breast carcinoma: a report from the National Cancer Data Base, 2004-2010," *JAMA Surg.* **149**, 1296–1305 (2014).
10. S. E. Singletary, "Surgical margins in patients with early-stage breast cancer treated with breast conservation therapy," *Am. J. Surg.* **184**, 383–393 (2002).
11. J. M. Jorns et al., "Intraoperative frozen section analysis of margins in breast conserving surgery significantly decreases reoperative rates: one-year experience at an ambulatory surgical center," *Am. J. Clin. Pathol.* **138**, 657–669 (2012).
12. E. K. Valdes et al., "Intra-operative touch preparation cytology; does it have a role in re-excision lumpectomy?" *Ann. Surg. Oncol.* **14**, 1045–1050 (2007).
13. K. Esbona, Z. Li, and L. G. Wilke, "Intraoperative imprint cytology and frozen section pathology for margin assessment in breast conservation surgery: a systematic review," *Ann. Surg. Oncol.* **19**, 3236–3245 (2012).
14. O. Riedl et al., "Intraoperative frozen section analysis for breast-conserving therapy in 1016 patients with breast cancer," *Eur. J. Surg. Oncol.* **35**, 264–270 (2009).
15. A. O. Saarela et al., "Determinants of positive histologic margins and residual tumor after lumpectomy for early breast cancer: a prospective study with special reference to touch preparation cytology," *J. Surg. Oncol.* **66**, 248–253 (1997).
16. J. M. Jorns et al., "Is intraoperative frozen section analysis of reexcision specimens of value in preventing reoperation in breast-conserving therapy?" *Am. J. Clin. Pathol.* **142**, 601–608 (2014).
17. J. C. Cendan, D. Coco, and E. M. Copeland III, "Accuracy of intraoperative frozen-section analysis of breast cancer lumpectomy-bed margins," *J. Am. Coll. Surg.* **201**, 194–198 (2005).

18. T. Osako et al., "Efficacy of intraoperative entire-circumferential frozen section analysis of lumpectomy margins during breast-conserving surgery for breast cancer," *Int. J. Clin. Oncol.* **20**, 1093–1101 (2015).
19. C. W. Barth et al., "Optimizing fresh specimen staining for rapid identification of tumor biomarkers during surgery," *Theranostics* **7**, 4722–4734 (2017).
20. S. C. Davis et al., "Topical dual-stain difference imaging for rapid intra-operative tumor identification in fresh specimens," *Opt. Lett.* **38**, 5184–5187 (2013).
21. S. Kang et al., "Microscopic investigation of topically applied nanoparticles for molecular imaging of fresh tissue surfaces," *J. Biophotonics* **11**, e201700246 (2018).
22. Y. Wang et al., "Surgical guidance via multiplexed molecular imaging of fresh tissues labeled with SERS-coded nanoparticles," *IEEE J. Sel. Top Quantum. Electron.* **22**(4), 6802911 (2016).
23. Y. Wang et al., "Quantitative molecular phenotyping with topically applied SERS nanoparticles for intraoperative guidance of breast cancer lumpectomy," *Sci. Rep.* **6**, 21242 (2016).
24. Y. W. Wang et al., "In vivo multiplexed molecular imaging of esophageal cancer via spectral endoscopy of topically applied SERS nanoparticles," *Biomed. Opt. Express* **6**, 3714–3723 (2015).
25. Y. W. Wang et al., "Raman-encoded molecular imaging with topically applied SERS nanoparticles for intraoperative guidance of lumpectomy," *Cancer Res.* **77**, 4506–4516 (2017).
26. Y. W. Wang et al., "High-speed Raman-encoded molecular imaging of freshly excised tissue surfaces with topically applied SERRS nanoparticles," *J. Biomed. Opt.* **23**, 046005 (2018).
27. O. Metzger-Filho et al., "Dissecting the heterogeneity of triple-negative breast cancer," *J. Clin. Oncol.* **30**, 1879–1887 (2012).
28. K. M. Hackman et al., "Polymeric micelles as carriers for nerve-highlighting fluorescent probe delivery," *Mol. Pharm.* **12**, 4386–4394 (2015).
29. J. J. Yim et al., "Optimization of a protease activated probe for optical surgical navigation," *Mol. Pharmaceut.* **15**, 750–758 (2018).
30. Y. Urano et al., "Rapid cancer detection by topically spraying a gamma-glutamyltranspeptidase-activated fluorescent probe," *Sci. Transl. Med.* **3**, 110ra119 (2011).
31. G. M. van Dam et al., "Intraoperative tumor-specific fluorescence imaging in ovarian cancer by folate receptor-alpha targeting: first in-human results," *Nat. Med.* **17**, 1315–1319 (2011).
32. S. M. Mahalingam et al., "Carbonic anhydrase IX-targeted near-infrared dye for fluorescence imaging of hypoxic tumors," *Bioconjug. Chem.* **29**, 3320–3331 (2018).
33. C. W. Barth and S. L. Gibbs, "Direct administration of nerve-specific contrast to improve nerve sparing radical prostatectomy," *Theranostics* **7**, 573–593 (2017).
34. K. S. Samkoe et al., "Toxicity and pharmacokinetic profile for single-dose injection of ABY-029: a fluorescent anti-EGFR synthetic affibody molecule for human use," *Mol. Imaging Biol.* **19**, 512–521 (2017).
35. W. S. Tummers et al., "Regulatory aspects of optical methods and exogenous targets for cancer detection," *Cancer Res.* **77**, 2197–2206 (2017).
36. S. Kennedy et al., "Optical breast cancer margin assessment: an observational study of the effects of tissue heterogeneity on optical contrast," *Breast Cancer Res.* **12**, R91 (2010).
37. L. G. Wilke et al., "Rapid noninvasive optical imaging of tissue composition in breast tumor margins," *Am. J. Surg.* **198**, 566–574 (2009).
38. R. Emmadi and E. L. Wiley, "Evaluation of resection margins in breast conservation therapy: the pathology perspective-past, present, and future," *Int. J. Surg. Oncol.* **2012**, 180259 (2012).

Biographies of the authors are not available.